Simultaneous Assessment of Mechanical Properties and Boundary Conditions Based on Digital Image Correlation

Roberto Fedele

Received: 17 October 2013 / Accepted: 21 July 2014 / Published online: 23 August 2014

Introduction

During the last years, high-accuracy, full field kinematic measurements at different observation scales provided by 2D Digital Image Correlation (DIC) procedures are being employed for an increasingly number of applications in material and structural mechanics, see e.g. [2–4]. Recent contributions range from civil engineering [5–8] to high temperature tests on metal alloys and ceramics for aggressive environments [9, 10]. In particular, the availability of full-field data allows one to monitor during non trivial tests small regions over the specimen surface, in which the phenomenon of interest turns out to be predominant (see also [11–14]). *Virtual* tests on a small sub-domain can thus be performed by assigning local boundary conditions, which integrate or even supersede the overall ones prescribed to the whole tested sample (typically, the reaction force).

Such local strategies are especially suitable for complex laboratory experiments, ad-hoc designed to generate strain and stress fields close to those expected under service [15–18]. In this respect, a careful distinction is needed between the material behavior and the observable, structural response. Overall boundary conditions prescribed to the specimen have to be regarded as uncertain, due to the gap between the ideal constraints, as usually described in mathematical models, and their "actual" behavior (e.g., in the presence of compliant supports).

In a previous paper [1], a numerical-experimental methodology was developed to estimate parameters governing the mixed mode response of an adhesive joint inside a composite assembly. Therein a local approach was proposed focusing on a Region-Of-Interest (ROI), for which (Dirichlet) boundary conditions were prescribed. Noise oscillations on boundary data (provided by DIC, see also [19]) propagated inside the ROI and affected the stress

R. Fedele (✉)
Department of Civil and Environmental Engineering (DICA),
Politecnico di Milano, Piazza Leonardo da Vinci
n. 32, 20133 Milan, Italy
e-mail: roberto.fedele@polimi.it

and strain distributions over the adherends and the traction profiles at the interface.

In this study, an improvement of the original strategy is presented. The boundary displacements to be prescribed along the ROI border at different instants are included as unknowns in the identification problem. The forward operator, based on a finite element discretization, is now regarded as a function of both the arguments, i.e. the cohesive parameters of the adhesive joint and the "actual" boundary displacements specifying the loading history. Also the cost (or objective) function to minimize, quantifying the discrepancy between DIC measurements and model predictions, includes displacements both along the boundary and inside the sub-domain.

The paper is organized as follows. Section "Debonding Experiments and their Finite Element Simulations" outlines the main features of the reference experiments and their simulations. Sensitivity analyses with respect to boundary conditions are illustrated in section "Sensitivity Analyses with Respect to Boundary Displacements and Cohesive Parameters". The novel extended formulation for the identification problem is presented in section "Extended Identification Problem", and the regularization provisions are discussed in section "Regularization Provisions". Section "Numerical Results" presents in detail the numerical exercises. Closing remarks and future prospects are gathered in section "Closing Remarks and Future Prospect".

Notation With reference to the problem domain Ω, the interior part, the outer border (the frontier, along which displacements are prescribed) and the closure will be denoted by symbols $\overset{\circ}{\Omega}$, $\partial\Omega$ and $\overline{\Omega} \equiv \overset{\circ}{\Omega} \cup \partial\Omega$, respectively. Partition of vector (or matrix) $\boldsymbol{X}$ into subvectors (or block matrices) $\boldsymbol{a}$ and $\boldsymbol{b}$ will be indicated by $\boldsymbol{X} = \{\boldsymbol{a} \,\vdots\, \boldsymbol{b}\}$ (or by $\boldsymbol{X} = \left[\boldsymbol{a} \,\vdots\, \boldsymbol{b}\right]$). $F(\boldsymbol{a}, \boldsymbol{b})$ is intended to emphasize the presence of two (vector) arguments simultaneously active for function F, whilst $F(\boldsymbol{a} \,|\, \boldsymbol{b})$ indicates that only the first argument $\boldsymbol{a}$ is active, the second *dummy* argument $\boldsymbol{b}$ being *frozen* and taken constant. Indices i and k will indicate time instants for pictures and steps of the extended procedure, respectively. The acronyms ROI, DIC and FE will denote the Region-Of-Interest, the 2D Digital Image Correlation procedure and the Finite Element method, respectively.

Debonding Experiments and their Finite Element Simulations

The main features of non-conventional tests on an adhesively bonded assembly, assumed herein as a methodological reference, and of its FE simulations are briefly outlined in what follows. For further details, the interested reader is referred to [1]. The experiments reported herein were conceived to characterize a structural (60-μm thick) adhesive layer, made of BMS 5–101 produced by 3M (commercial denomination AF163 degree 10), joining a (1.4-mm thick) laminate skin and a Z-shaped reinforcement (stringer), both made of GLARE composites for aerospace applications (see e.g. [20]). Non-conventional tests were designed and performed on rectangular joined specimens (surface area: 297 $\times$ 50 mm^2) to generate within the adhesive complex stress and strain states close to those expected under service, see Fig. 1. The specimen was constrained at the ends, whilst an increasing vertical displacement was prescribed by grips to the upper part of the reinforcement till to induce complete debonding under mixed mode conditions, resulting in the overall reaction history of Fig. 2.

A small region on the specimen surface around the adhesive layer (of area approximately equal to 0.6 $\times$ 1.3 mm^2) was selected as ROI and optically monitored during the tests. The camera was equipped by a long-distance zoom objective and motorized stages to follow in real time the ROI during motion. Pictures were sampled at two different rates: initially a slow rate was used, while the frequency was increased up to 0.5 Hz when crack appeared along the joint.

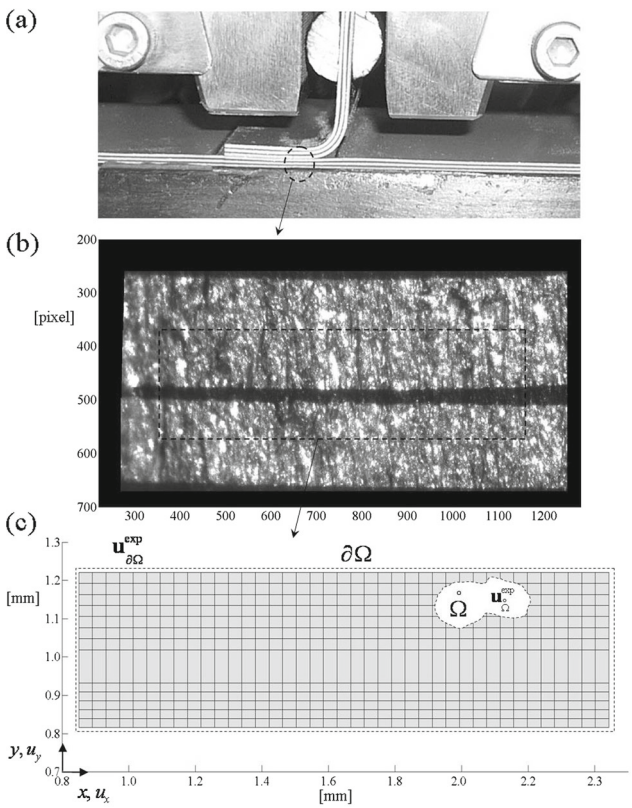

Fig. 1 Z-shaped GLARE sample including the adhesive joint in **(a)**, reference picture at the microscale acquired by a zoomed camera for DIC analyses in **(b)**, FE discretization adopted for mechanical analyses in **(c)**

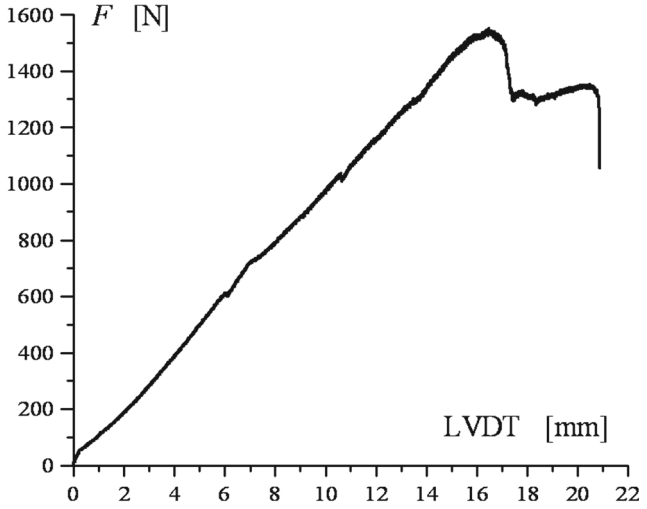

Fig. 2 Experimental response in terms of vertical reaction force versus overall prescribed displacement

Selected digital images were post-processed to reduce rigid body motion components still present in them.

To reconstruct displacements on the basis of digital images, recourse was made to Correli©, a 2D DIC code based on a Galerkin, FE approach with Q4-(bilinear) shape functions [21]. Full field measurements were available at $n_t = 19$ instants during the test. The behavior of aluminum substrates (cold-rolled 2024-T3 alloy) was described according to Ramberg-Osgood's model, see e.g. [22]. All parameters governing the response of the aluminum alloy sheets were assumed to be known *a priori* with a sufficient accuracy, playing in the proposed inverse methodology the role of a diffuse "load cell".

To describe the joint response under mixed-mode loading conditions, the exponential relationship proposed in [23] was adopted, namely:

$$T_n = \frac{\phi_n}{\delta_n}\left(\frac{\Delta_n}{\delta_n}\right)\exp\left[-\frac{\Delta_n}{\delta_n}\right]\exp\left[-\frac{\Delta_t^2}{\delta_t^2}\right]$$
$$T_t = \frac{2\,r\,\phi_n}{\delta_t}\left(\frac{\Delta_t}{\delta_t}\right)\left(1+\frac{\Delta_n}{\delta_n}\right)\exp\left[-\frac{\Delta_n}{\delta_n}\right]\exp\left[-\frac{\Delta_t^2}{\delta_t^2}\right] \tag{1}$$

where T_n and T_t , Δ_n and Δ_t denote normal and tan-gential components of traction and displacement vectors, respectively. Symbols δ_n, δ_t , ϕ_n and $r \cdot \phi_n$ designate the normal and tangential characteristic lengths, and the works-of-separation (for a unit surface) under pure Mode I (peel) and Mode II (shear), respectively, being $r = \phi_t / \phi_n$ the (non-dimensional) ratio between the tangential and nor-mal works-of-separations, herein assumed a priori on the basis of literature data (see also [24, 25]). In what follows the three unknown parameters governing the adhesive layer behavior are gathered in vector $\boldsymbol{x} = \{\phi_n, \delta_n, \delta_t\}^T$.

It is worth emphasizing that, over the optically monitored surface, the out-of-plane component of traction vector is null and plane stress conditions are met. Actually, inside the tested sample stress triaxiality varies through the thickness, in such a way that plane strain conditions are approached over the middle plane. As a consequence the crack front cannot be cylindrical and noteworthy exhibits along the thickness a convex profile, more or less pronounced. Unfortunately, three dimensional modelling of a suitable volume of interest, including the whole crack front, is herein prevented by lack of bulk kinematic data, needed to drive the simulation as prescribed boundary conditions. These information could be provided by scanning in real time the loaded sample by means of an X-ray microCT, and processing the tomography sequence by 3D-Volume DIC [26]. As a valid alternative to simulate the overall fracture response of thick samples (typically the reaction force, as in [27]), the plane strain approximation is often being adopted for its simplicity and reduced computing effort, although a proper assessment of the prediction errors implied by this simplifying assumption is often omitted. In particular, for the problem in point forward analyses based on the plane strain approximation have generated kinematic residuals (i.e. discrepancies with respect to experimental displacements detected over the outer surface) largely exceeding those predicted by their plane stress counterparts, even though the cohesive properties of the joint and the prescribed boundary conditions remained the same. This circumstance reveals that important modelling errors are implied by the plane strain assumption when referred to displacements of the outer surface. Moreover, in the present inverse procedure plane strain approximation has led to interface tractions markedly higher than their counterparts estimated under plane stress (and even than literature data). Therefore, for the present study the plane stress approximation was strongly preferred. For the readers' convenience, a brief Appendix was provided at the end of the paper, summaring the results of comparative forward and inverse analyses performed on a different experimental configuration.

In the considered problem, the monitored subdomain $\Omega \subset \mathbb{R}^2$ over the free specimen surface was covered by $n_{\text{el}} = 570$ four-noded finite elements $\left(\Omega = \bigcup_{e=1}^{n_{\text{el}}} \Omega_{(e)}\right)$. The adhesive layer was discretized by means of 39 finite-thickness interface elements, equipped with the cohesive law specified in equation (1). The discretized equilibrium equation at instant i reads

$$\boldsymbol{R}^i \equiv \boldsymbol{F}^i_{\text{int}}\left(\boldsymbol{u}^i_{\underset{\Omega}{\circ}}\right) - \boldsymbol{F}^i_{\text{ext}} = \boldsymbol{0} \tag{2}$$

where $\boldsymbol{F}^i_{\text{ext}}$ denotes the vector of external forces. Displacements implicitly defined by equation (2) as usual concern only the free nodes in the interior domain and are computed

by Newton-Raphson iterations. The nonlinear relationship between the unknown model parameters and the selected measurable quantities in the interior part of the ROI is referred to as forward operator, and denoted by symbol $\underset{\Omega}{\overset{\circ}{\boldsymbol{u}}}^{\text{comp}}(\boldsymbol{x}, \boldsymbol{u}_{\partial\Omega}$. Herein the two active arguments of the above operator are emphasized, namely the cohesive properties of the interface $\boldsymbol{x} = \{\phi_n, \delta_n, \delta_t\}^T$, and the $(n_t \times 2\, n_{\partial\Omega})$-dimensional vector $\boldsymbol{u}_{\partial\Omega}$ including boundary displacements at different measurement instants $i = 1, ..., n_t \equiv 19$, in what follows both gathered in the augmented parameter vector $\boldsymbol{X} = \{\boldsymbol{x}^T \,\vdots\, \boldsymbol{u}_{\partial\Omega}^T\}^T$.

Sensitivity Analyses with Respect to Boundary Displacements and Cohesive Parameters

Derivatives of the displacement field $\boldsymbol{u} \equiv \{u_x, u_y\}^T$ with respect to the unknown parameter vector $\boldsymbol{X}$ are needed both for the optimal design of the experiments, and to compute gradients required in the first-order minimization procedure [28]. Only a few hints are proposed in what follows, emphasizing the extension of sensitivity computation to boundary displacements.

By differentiating the discretized equilibrium equations at time instant i in equation (2) and partitioning the parameter vector as above, the following auxiliar equation holds $\left(\text{being for simplicity } \boldsymbol{u}^i \equiv \underset{\Omega}{\overset{\circ}{\boldsymbol{u}}}^i\right)$:

$$\boldsymbol{K}_{\boldsymbol{u}}^i \cdot \left[\frac{\partial \boldsymbol{u}^i}{\partial \boldsymbol{x}^T} \,\vdots\, \frac{\partial \boldsymbol{u}^i}{\partial \boldsymbol{u}_{\partial\Omega}^{i\,T}}\right] = -\left[\frac{\partial \boldsymbol{R}^i}{\partial \boldsymbol{x}^T} \,\vdots\, \frac{\partial \boldsymbol{R}^i}{\partial \boldsymbol{u}_{\partial\Omega}^{i\,T}}\right] \tag{3}$$

At the current time step i $(i = 1, ..., n_t)$, the internal force vector $\boldsymbol{F}_{\text{int}}^i$, the overall stiffness matrix $\boldsymbol{K}_{\boldsymbol{u}}^i$, the pseudo-load matrices at the r.h.s. are defined in the order as follows (see also [29]):

$$\boldsymbol{F}_{\text{int}}^i = \mathop{\mathbf{A}}_{e=1}^{n_{\text{el}}} \int_{\Omega_{(e)}} \boldsymbol{B}^T \boldsymbol{\sigma}^i \left(\underset{\Omega}{\overset{\circ}{\boldsymbol{u}}}^i(\boldsymbol{X}), \boldsymbol{X}, \boldsymbol{u}_{\partial\Omega}^i\right) d\Omega_{(e)} \tag{4a}$$

$$\boldsymbol{K}_{\boldsymbol{u}}^i = \frac{\partial \boldsymbol{R}^i}{\partial \boldsymbol{u}^{i\,T}} = \mathop{\mathbf{A}}_{e=1}^{n_{\text{el}}} \int_{\Omega_{(e)}} \boldsymbol{B}^T \frac{\partial \boldsymbol{\sigma}^i}{\partial \boldsymbol{u}^{i\,T}} d\Omega_{(e)} \tag{4b}$$

$$\frac{\partial \boldsymbol{R}^i}{\partial \boldsymbol{x}^T} = \mathop{\mathbf{A}}_{e=1}^{n_{\text{el}}} \int_{\Omega_{(e)}} \boldsymbol{B}^T \frac{\partial \boldsymbol{\sigma}^i}{\partial \boldsymbol{x}^T} d\Omega_{(e)} \;;$$

$$\frac{\partial \boldsymbol{R}^i}{\partial (\boldsymbol{u}_{\partial\Omega}^i)_m} = \mathop{\mathbf{A}}_{e=1}^{n_{\text{el}}} \boldsymbol{k}^{(e)}(:, m^{(e)})\Big] \tag{4c}$$

where: $\mathop{\mathbf{A}}_{e=1}^{n_{\text{el}}}$ indicates the assembly operator acting on the (e)-th element, $e = 1, ..., n_{\text{el}}$, and gathering local contributions into the residual vector $\boldsymbol{R}^i$ of equation (2); $\boldsymbol{B}$, $\boldsymbol{\sigma}^i$ and $\boldsymbol{k}^{(e)}(:, m^{(e)})$ denote the compatibility matrix, the current value of local stress vector and the $m^{(e)}$-th (in the local convention) column of the (e)-th element stiffness matrix at instant i, relevant to the m-th degree-of-freedom in the global convention, respectively.

To compute sensitivities with respect to the m-th component of boundary displacement vector at instant i, say $\left(\boldsymbol{u}_{\partial\Omega}^i\right)_m$, contributions from no more than two finite elements (having in common that boundary node) are required for assembling the pseudo-load matrix. Sensitivity trivially equals one at the reference node, whilst it vanishes along the remaining boundary nodes. Once that the inverse coefficient matrix $\boldsymbol{K}_{\boldsymbol{u}}^{-1}$ is factorized and stored, only matrix multiplications are required to solve equation (3), and the sensitivity computation turns out to be very fast despite of the high-dimensionality of pseudo-load matrix at the r.h.s. in equation (3).

Figure 3 shows the sensitivity of horizontal displacement field u_x at instant $i = 1$, with respect to the horizontal displacement at the upper left corner of the domain Ω (the unitary value results out of scale). Sensitivity emanates from the boundary node and diffuses over a wide part of the modeled domain.

Extended Identification Problem

In the original inverse methodology presented in [1], experimental displacements provided by DIC at different measurement instants, gathered in the $(n_t \times 2\, n_{\partial\Omega})$-dimensional vector $\boldsymbol{u}_{\partial\Omega}^{\text{exp}}$, were *deterministically* prescribed along the outer boundary $\partial\Omega$ of the monitored subdomain. Then the cohesive parameters of the joint were estimated as follows:

$$\widehat{\boldsymbol{x}} = \arg\min_{\boldsymbol{x}} \left\| \boldsymbol{S}_1 \cdot \left[\underset{\Omega}{\overset{\circ}{\boldsymbol{u}}}^{\text{exp}} - \underset{\Omega}{\overset{\circ}{\boldsymbol{u}}}^{\text{comp}}(\boldsymbol{x} \,\big|\, \boldsymbol{u}_{\partial\Omega}^{\text{exp}})\right]\right\|_{\boldsymbol{W}}^2 \tag{5}$$

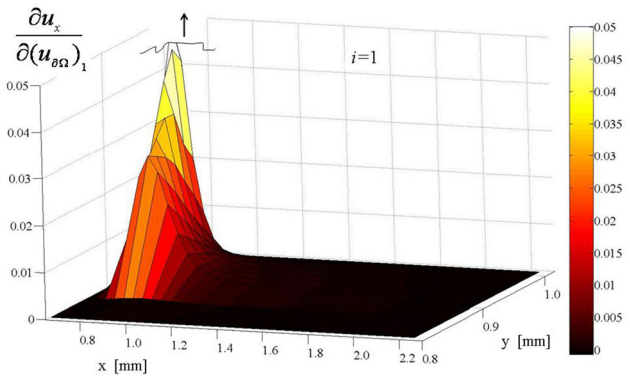

Fig. 3 Sensitivity of displacement field u_x at instant $i = 1$ with respect to horizontal boundary displacement $\left(u_{\partial\Omega}^1\right)_1$ at the upper left corner of the discretized subdomain. At that boundary node, sensitivity equals one (out of scale)

In equation (5) the forward operator results as a function of the cohesive parameters only (herein $n_x = 3$). Displacements at nodes located closely to the joint were selected via the Boolean matrix $\boldsymbol{S}_1$ (weighting matrix $\boldsymbol{W}$ will be discussed later). Vectors $\boldsymbol{u}_{\overset{\circ}{\Omega}}$ and $\boldsymbol{u}^{\exp}_{\partial\Omega}$ orderly gather contributions relevant to different time instants i ($i = 1, ..., n_t$).

The main disadvantage of the above formulation is that boundary data estimated by DIC turns out to be noisy, and such noise perturbations propagate from the outer border toward the inner part of the ROI, making hardly legible the stress and strain maps and presumably altering the traction profiles. This situation is made even worse by the slender geometry of the ROI, and by the nonlinear behavior of the aluminum adherends.

To tackle these drawbacks, the identification problem in equation (5) can be extended or generalized by relaxing in some way the constraint $\boldsymbol{u}_{\partial\Omega} = \boldsymbol{u}^{\exp}_{\partial\Omega}$, implicitly assumed for the forward modeling. Since DIC measurements are noisy, it is fully reasonable to admit non vanishing residuals also along the border, and not only in the interior part of the ROI. In this perspective, the vector of measurable quantities can be augmented to encompass displacements belonging to the whole ROI, i.e. to the closure $\overline{\Omega} \equiv \overset{\circ}{\Omega} \cup \partial\Omega$. Such measurable quantities are expected to be close to the ones provided by DIC, but not exactly coincident with them due to the presence of noise and model error. The augmented parameter vector $\boldsymbol{X} = \{\boldsymbol{x}^T \,\vdots\, \boldsymbol{u}^T_{\partial\Omega}\}^T$, including both the cohesive parameters (which are not time dependent) and the "actual" history of boundary displacements during the test, could in principle be estimated by the formally unchanged formulation of equation (5), in which data and parameter vector are augmented, namely:

$$\widehat{\boldsymbol{X}} = \arg\min_{\boldsymbol{X}} \left\{ \left\| \boldsymbol{S}_1 \cdot \left[\boldsymbol{u}^{\exp}_{\overset{\circ}{\Omega}} - \boldsymbol{u}^{\mathrm{comp}}_{\overset{\circ}{\Omega}}(\boldsymbol{x}, \boldsymbol{u}_{\partial\Omega}) \right] \right\|^2_{\boldsymbol{W}} + \left\| \boldsymbol{u}^{\exp}_{\partial\Omega} - \boldsymbol{u}_{\partial\Omega} \right\|^2_{\boldsymbol{W}} \right\} \tag{6}$$

If n_t denotes the available time instants, the dimension of the parameter space in equation (6) results $n_X = n_x + n_t \times 2\, n_{\partial\Omega} = 3 + 19 \cdot 208 = 3955$! Unfortunately, the minimization process with such a number of simultaneous unknowns is likely to become prohibitive in the presence of a nonlinear and non-convex objective function, with an unstable dependence of the solution vector on data possibly endowed by solution multiplicity.

To drastically decrease the problem dimensionality of equation (6) and increase robustness of the ill-posed inverse procedure, a sequentially decoupled strategy is then proposed. Recourse is made to an alternating minimization procedure (see e.g. [30]), in which minimization is performed iteratively through restricted or partial minimizations, with decoupling in the step among mechanical parameters and boundary displacements. At the k-th step ($k > 1$), two stages are then considered according to the following pseudo-code:

Stage 1,

$$\begin{aligned} & \boldsymbol{x}_0 \equiv \widehat{\boldsymbol{x}}^{(k-1)} \\ & \widehat{\boldsymbol{x}}^{(k)} = \arg\min_{\boldsymbol{x}} \; \omega_1\left(\boldsymbol{x} \,\middle|\, \boldsymbol{u}^{(k-1)}_{\partial\Omega}\right) \\ & \omega_1 = \left\| \boldsymbol{S}_1 \cdot \left\{ \boldsymbol{u}^{\exp}_{\overset{\circ}{\Omega}} - \boldsymbol{u}^{\mathrm{comp}}_{\overset{\circ}{\Omega}}\left(\boldsymbol{x} \,\middle|\, \boldsymbol{u}^{(k-1)}_{\partial\Omega}\right) \right\} \right\|^2_{\boldsymbol{W}} \\ & \qquad + c_x \cdot R_x(\boldsymbol{x}) \end{aligned} \tag{7}$$

Stage 2,

$$\begin{aligned} & \boldsymbol{u}_{\partial\Omega\,0} \equiv \boldsymbol{u}^{k-1}_{\partial\Omega} \\ & \text{DO } \bar{i} = 1 : n_t \\ & \quad \widehat{\boldsymbol{u}}^{\bar{i},(k)}_{\partial\Omega} = \arg\min_{\boldsymbol{u}^{\bar{i}}_{\partial\Omega}} \; \omega_2\left(\boldsymbol{u}^{\bar{i},\star}_{\partial\Omega} \,\middle|\, \widehat{\boldsymbol{x}}^{(k)} \right) \\ & \quad \omega_2 = \left\| \boldsymbol{u}^{\exp}_{\overset{\circ}{\Omega}} - \boldsymbol{u}^{\mathrm{comp}}_{\overset{\circ}{\Omega}}\left(\boldsymbol{u}^{\bar{i},\star}_{\partial\Omega} \,\middle|\, \widehat{\boldsymbol{x}}^{(k)} \right) \right\|^2_{\boldsymbol{W}} \\ & \qquad + \left\| \boldsymbol{u}^{\exp}_{\partial\Omega} - \boldsymbol{u}^{\bar{i},\star}_{\partial\Omega} \right\|^2_{\boldsymbol{W}} \\ & \qquad + c_u \cdot R_u\left(\boldsymbol{u}^{\bar{i}}_{\partial\Omega}\right) \\ & \quad \boldsymbol{u}^{\bar{i},\star}_{\partial\Omega} \equiv \left\{ \widehat{\boldsymbol{u}}^{1,(k)}_{\partial\Omega}; ...; \widehat{\boldsymbol{u}}^{\bar{i}-1,(k)}_{\partial\Omega}; \boldsymbol{u}^{\bar{i}}_{\partial\Omega}; \right. \\ & \qquad \left. \widehat{\boldsymbol{u}}^{\bar{i}+1,(k-1)}_{\partial\Omega}; ...; \boldsymbol{u}^{n_t,(k-1)}_{\partial\Omega} \right\} \\ & \text{END DO} \\ & \widehat{\boldsymbol{u}}^{(k)}_{\partial\Omega} \equiv \boldsymbol{u}^{n_t,\star}_{\partial\Omega} \\ & k = k + 1 \end{aligned} \tag{8}$$

To avoid a cumbersome notation, in equations (7)-(8) kinematic quantities relevant to n_t time instants are intended to be orderly gathered in vectors $\boldsymbol{u}_{\overset{\circ}{\Omega}}$ and $\boldsymbol{u}_{\partial\Omega}$. Moreover, vector $\boldsymbol{u}^{\bar{i},\star}_{\partial\Omega}$ includes the boundary displacements estimated at the previous step $k-1$, sequentially updated during Stage 2; symbols $R_x(\boldsymbol{x})$ and $R_u\left(\boldsymbol{u}^{\bar{i}}_{\partial\Omega}\right)$ denote nonnegative regularization terms (to be discussed later), weighted by penalty factors $c_x, c_u \geq 0$, respectively. Weighting matrix $\boldsymbol{W}$ scales and makes non-dimensional the kinematic residuals, being $\| \boldsymbol{u} \|^2_{\boldsymbol{W}} \equiv \boldsymbol{u}^T \boldsymbol{W}^{-1} \boldsymbol{u}$: its diagonal entries are set equal to the maximum experimental displacement in absolute value, separately for each component (horizontal or vertical) and time instant, to make comparable the different contributions.

At each Stage the optimal parameters are obtained by minimizing a suitable discrepancy norm (objective or cost function), see e.g. [16, 17]. During Stage 1, exclusively the most sensitive displacements (closely to the adhesive joint)

are included in the objective function to minimize (selected through the Boolean matrix $\boldsymbol{S}_1$), consistently with the original procedure. At the first step ($k = 1$), Stage 1 is initialized with a reasonable guess $\boldsymbol{x}_0$ for the cohesive parameters provided by the user, whilst the boundary displacements are assumed to be trivially coincident with the experimental (noisy) values provided by DIC, namely $\boldsymbol{u}_{\partial\Omega\,0} \equiv \boldsymbol{u}^{\exp}_{\partial\Omega}$, and *frozen*. Moreover, as clarified later, the regularization provision R_x does not affect the results at the first step. These assumptions imply that, at Stage 1, the initial estimate of cohesive properties equals $\widehat{\boldsymbol{x}}^{\mathrm{NR}}$ achieved through the original inverse procedure in equation (5). For the estimation of the cohesive parameters $\boldsymbol{x}$ through equation (7), first a (zero-order, derivative-free) direct search is used to avoid local minima (the Nelder and Mead Simplex), followed by a gradient-based first-order minimization (Trust Region Method) to refine solution estimates.

At Stage 2, equation (8), while the cohesive parameters are set equal to those estimated at the previous Stage 1, i.e. $\boldsymbol{x} \equiv \widehat{\boldsymbol{x}}^k$, and *frozen*, the history of boundary data is updated. As a further simplification, displacements at the frontier relevant to the one measurement instant only, say $\boldsymbol{u}^{\bar{i}}_{\partial\Omega}$, are sequentially assumed as simultaneous unknowns ($2\,n_{\partial\Omega} = 208$) in the same minimization process. Objective function ω_2 to minimize now includes all kinematic data available in $\overline{\Omega}$. Vector $\boldsymbol{u}^{\mathrm{comp}}_{\mathring{\Omega}}$ gathers displacements provided by the FE model along the whole loading history, specified by suitable boundary conditions at n_t instants ordered in vector $\boldsymbol{u}^{\bar{i},\star}_{\partial\Omega}$. Besides the active argument $\boldsymbol{u}^{\bar{i}}_{\partial\Omega}$, vector $\boldsymbol{u}^{\bar{i},\star}_{\partial\Omega}$ driving the simulation includes *frozen* boundary conditions at remaining instants $i \neq \bar{i}$, either updated in the current DO loop ($i < \bar{i}$), or still equal ($i > \bar{i}$) to the estimates at previous step ($k - 1$) (symbol ";" in equation (8) indicates vertical disposition). When convergence is achieved by Trust Region algorithm (40 iterations at maximum are allowed for, as a compromise between solution accuracy and reduced computing time), the minimization process begins for displacements at the subsequent instant $\bar{i} + 1$, being always unchanged the cohesive parameters. Finally, Stage 2 is terminated when boundary data relevant to all the available n_t instants have been updated, gathered in vector $\widehat{\boldsymbol{u}}^{(k)}_{\partial\Omega}$, and a new step $k + 1$ can start. The de-coupled two-stage scheme presented above, equations (7) and (8), is repeated sequentially along several steps run by index k, till residual stabilization is ascertained from objective function evaluations.

In conclusion, it is worth emphasizing what follows: (i) most of the algorithms nowadays available for nonlinear and nonconvex minimisation (see e.g. [31]) are conceived and tested for a few hundred unknowns at maximum, and their use in problems with a higher dimensionality is not corroborated by a sufficiently wide expertise; (ii) in another identification study of the same Author [17], the de-coupled estimation of different parameter subsets, endowed by a consistent partition of data, has allowed to significantly improve the results, especially when noise levels were increased.

Regularization Provisions

In the extended inverse problem, equations (7) and (8), two regularization provisions were introduced, labeled in what follows as (a) and (b), the former concerning the cohesive parameters, the latter regularity of boundary data. In order to preserve the constraint-free formulation, herein recourse was made to a penalty approach, i.e. the regularizing conditions (a) and (b) are included explicitly in the cost functions as further addenda to minimize, enforced by nonnegative penalty factors c_x and c_u at Stages 1 and 2, equations (7) and (8) respectively. Their derivatives, required for gradient based minimization algorithms, can be easily computed through the chain rule on the basis of displacement sensitivities already available through equation (3).

(a) Neumann condition along the crack path Condition (*a*) can be regarded as an intriguing provision when dealing with full-field kinematic data. As a matter of fact, sometimes a macroscopic crack lying along the joint may be recognized without ambiguities in digital images. In the present case, during the experimental test the light of illumination lamps was passing from one side to another of the sample, through the crack opening along the joint, and this detail was detected by the camera. From a mechanical standpoint the debonded part of the joint is expected to be traction free, and locally one has $T_n = T_t = 0$: this condition trivially implies a null internal force vector $\boldsymbol{F}_{\mathrm{int}}$ (with size 8×1) in the same location of the discretized interface. However, the calibrated FE model may predict tractions not exactly vanishing at the same location of the joint, due to the presence of noise on processed data and inaccuracies in forward and inverse modelling. This equilibrium condition represents therefore a further constraint available, to be prescribed *explicitly* along the severe convergence process (during which even the boundary conditions

Table 1 Synthetic data at varying the noise standard deviation and relevant 99 % confidence intervals. Objective functions ω_1 and ω_2 before ($k = 1$) and after ($k = 9$) the extended identification procedure

noise (pixel)	ω_1 at k = 1	ω_1 at k = 9	ω_2 at k = 1	ω_2 at k = 9
$[-0.1, +0.1]$	287.241	0.018484	0.889531	0.230670
$[-0.2, +0.2]$	212.375	0.078564	3.21092	0.814518
$[-0.3, +0.3]$	133.785	0.185585	7.95335	2.02478

Table 2 Synthetic data over $\overline{\Omega}$ corrupted by additive random noise. Estimates of cohesive parameters $\boldsymbol{x}^{\mathrm{R}}$ at varying the noise level and average error with respect to a priori known values (along the first row)

noise (pixel)	ϕ_n [GPa $\cdot$ μm]	δ_n [μm]	δ_t [μm]	mean error
no	2.032	8.721	71.04	no
$[-0.1, +0.1]$	1.961	8.724	73.09	2.12 %
$[-0.2, +0.2]$	1.703	8.134	64.65	10.6 %
$[-0.3, +0.3]$	1.826	7.043	59.85	15 %

are iteratively updated). A further difficulty is due to the fact that herein the exponential relationship in equation (1) is used for the joint, leading to interface tractions which do not rigorously vanish when increasing the displacement jumps, and the above constraint on $\boldsymbol{F}_{\mathrm{int}}$ should be relaxed in some way. Let $(\overline{e})$ denote the interface element in point, and $\overline{i}$ the selected time instant. The following inequality is then considered:

$$|\boldsymbol{F}_{\mathrm{int}}^{(\overline{e})}(\boldsymbol{x}, \boldsymbol{u}^{(\overline{e}),\overline{i}})| \leq \boldsymbol{c}_F \tag{9}$$

In equation (9) each component of the internal force vector (in absolute value) at (e)-th interface element is required to be lower than a given threshold, at an assigned time instant $\overline{i}$. The a priori selection of the above threshold vector $\boldsymbol{c}_F$ may appear somewhat arbitrary or subjective. However, in the present case a rather intuitive and simple tuning strategy can be envisaged. In fact, threshold $\boldsymbol{c}_F$ is selected as the minimum nodal force which does not affect the original unconstrained identification problem in equation (5): therefore, $\boldsymbol{c}_F \equiv |\boldsymbol{F}_{\mathrm{int}}^{(\overline{e})}(\widehat{\boldsymbol{x}}^{\mathrm{NR}})|$ is assumed, where $\widehat{\boldsymbol{x}}^{\mathrm{NR}}$ denotes the optimal parameter estimate provided by the original, not regularized formulation. Due to the adopted tuning strategy, during the first step (at $k = 1$) of the extended procedure, above inequality is satisfied, and the solution at Stage 1 equals that of the original inverse problem.

To formulate the inequality constraint of equation (9) in a penalty form, the following mathematical artifice is considered (see e.g. [32]): $g(x) \geq 0 \Rightarrow (|g(x)| - g(x)) = 0$. Then one has: $\boldsymbol{g} = (-|\boldsymbol{F}_{\mathrm{int}}^{(\overline{e})}| + \boldsymbol{c}_F) \geq \boldsymbol{0} \Rightarrow R_x = 1/F_0^2 \cdot \| \, |\boldsymbol{g}| - \boldsymbol{g} \, \|^2 = 0$, where the reference nodal force F_0 makes this expression non-dimensional, consistently with the discrepancy norm.

(b) Orthogonal basis for boundary displacements The second regularizing provision herein adopted concerns the boundary data. In the extended formulation the unknown boundary displacements at different instants are constrained (through suitable projection operators) to belong to the space spanned by a set of orthogonal Čebyšhëv polynomials (of the I kind), properly selected by the user. Boundary displacements can then be expressed as a linear combination of the adopted truncated basis functions defined over the whole ROI (as it occurs in some spectral methods). This kind of polynomials exhibit peculiar features, namely stability with respect to data, even when a regular grid is used for least-square fitting, and fast convergence, in the sense that very few terms are usually needed, see e.g. [33]. This regularity condition for the boundary displacements at a given instant $\overline{i}$ can be easily expressed by formulae as follows:

$$\boldsymbol{P}_{\perp} \cdot \boldsymbol{u}_{\partial\Omega}^{\overline{i}} = \boldsymbol{0} \tag{10}$$

where $\boldsymbol{P}_{\perp}$ is the orthogonal projection operator, with respect to the space spanned by the adopted truncated basis. Consistently, the relevant regularization term is built as follows (exploiting projector idempotency): $R_u = 1/L_0^2 \, \boldsymbol{u}_{\partial\Omega}^{\overline{i}\,T} \boldsymbol{P}_{\perp} \boldsymbol{u}_{\partial\Omega}^{\overline{i}} \geq 0$, where symbol L_0 denotes a reference length. It is worth emphasizing that the penalty factor

Table 3 Synthetic data at varying the noise level. Mean and maximum value for the normalized discrepancy between the estimated vertical displacement over Ω and its noiseless counterpart at instant $i = 3$ during the test, before ($k = 1$) and after ($k = 9$) the extended identification procedure

noise (pixel)	mean at k = 1	mean at k = 9	max at k = 1	max at k = 9
$[-0.1, +0.1]$	0.01075	0.001941	0.08126	0.03893
$[-0.2, +0.2]$	0.02367	0.006788	0.2424	0.1413
$[-0.3, +0.3]$	0.03388	0.009212	0.3230	0.1380

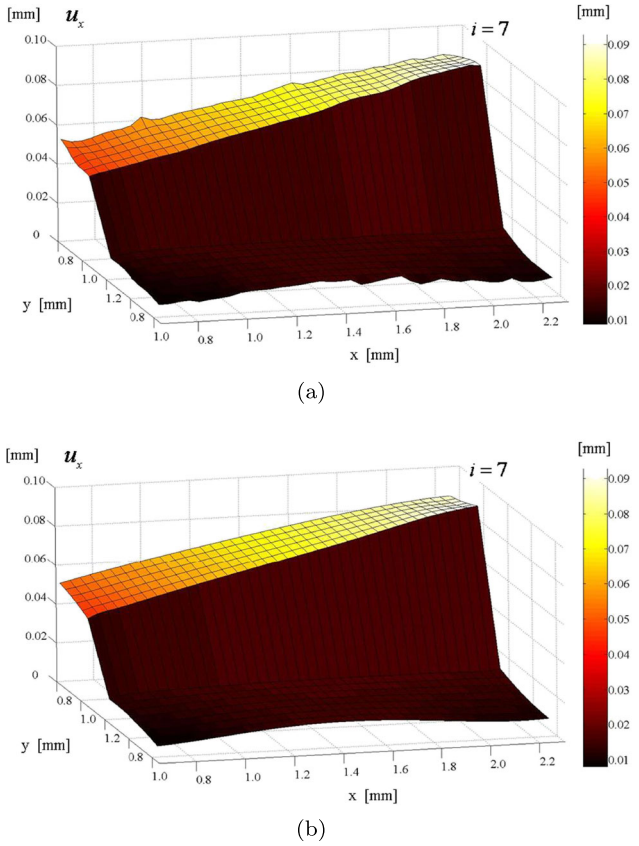

Fig. 4 Horizontal displacement component (parallel to the joint) computed by the FE model at instant $i = 7$, estimated by: the original identification procedure, in (**a**); the extended strategy, in (**b**)

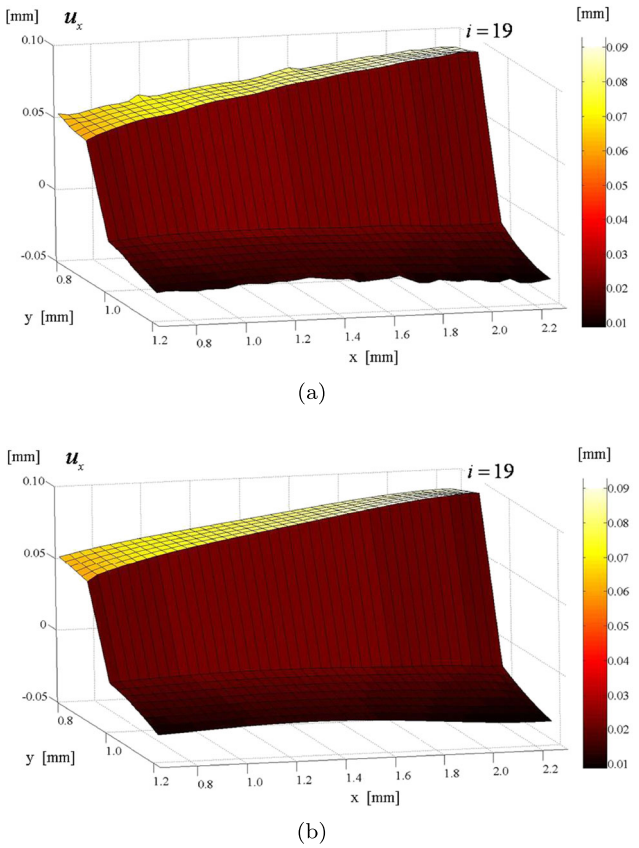

Fig. 5 Horizontal displacement component (parallel to the joint) computed by the FE model at instant $i = 19$, estimated by: the original identification procedure, in **(a)**; the extended strategy in **(b)**

c_u in equation (8) allows for a relaxation of the above constraint.

Numerical Results

Synthetic data The proposed methodology was first validated through *pseudo-experimental* data, i.e. synthetic data generated by parameters $\overline{\boldsymbol{X}} = \{\overline{\boldsymbol{x}}^T \,\vdots\, \overline{\boldsymbol{u}}^T_{\partial\Omega}\}^T$ assumed to be known a priori. To this purpose a synthetic history of boundary displacements $\boldsymbol{u}_{\partial\Omega}$ was selected, consistently with Čebyšhëv polynomials adopted for boundary data regularization and generating in the modeled subdomain mixed mode loading conditions for the joint. Then, on the basis of the above loading history and of assigned cohesive parameters $\boldsymbol{x}$, displacements in the interior domain were computed by the forward operator $\boldsymbol{u}^{\text{comp}}_{\overset{\circ}{\Omega}}\left(\overline{\boldsymbol{x}} \,\middle|\, \overline{\boldsymbol{u}}_{\partial\Omega}\right)$. In this way, a complete set of synthetic kinematic measurements over $\overline{\Omega}$ was generated. Thereafter, such kinematic fields were corrupted by artificial noise both in the interior domain $\overset{\circ}{\Omega}$ and along the outer boundary $\partial\Omega$, to simulate the experimental scatter. Gaussian perturbations with null mean value and prescribed standard deviation (no spatial correlation considered) were added to each nodal displacement as follows:

$$\boldsymbol{u}^{\text{exp}}_{\overline{\Omega}} = \left[\, \boldsymbol{u}^{\text{comp}}_{\overset{\circ}{\Omega}}\left(\overline{\boldsymbol{x}} \,\middle|\, \overline{\boldsymbol{u}}_{\partial\Omega}\right) \,\vdots\, \overline{\boldsymbol{u}}_{\partial\Omega} \,\right] + \boldsymbol{e} \tag{11}$$

Preliminarily, the possible dependence of parameter estimates on the initialization vector (at step $k = 1$) was investigated on the basis of noiseless data. Different initializations of cohesive parameters $\widehat{\boldsymbol{x}}_0$ were then considered at Stage 1, also because a priori information on joint properties inside the final manufact are likely to be poor. In all exercises, by the inverse procedure the correct solutions were fastly recovered in a few steps. It is worth noting that, during the first step $k = 1$, stage 2 is initialized by the available pseudo-experimental data set $\boldsymbol{u}^{\text{exp}}_{\partial\Omega}$, coincident with the boundary conditions driving the test simulation at previous Stage 1 and entering the objective function ω_2. This choice, endowed by reasonable block constraints on the solution vector (equal to ± 5 pixel for each nodal displacement), avoided premature convergence to secondary minima.

To assess robustness of the inverse procedure, progressively higher noise levels were considered for the synthetic

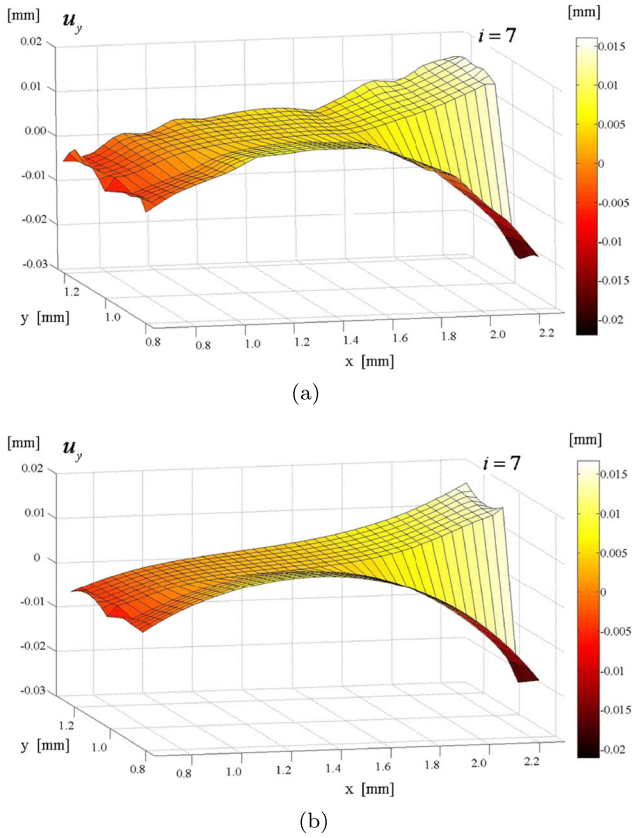

Fig. 6 Vertical displacement component (normally to the joint) computed by the FE model at instant $i = 7$, estimated by: the original identification procedure, in (**a**); the extended strategy, in (**b**)

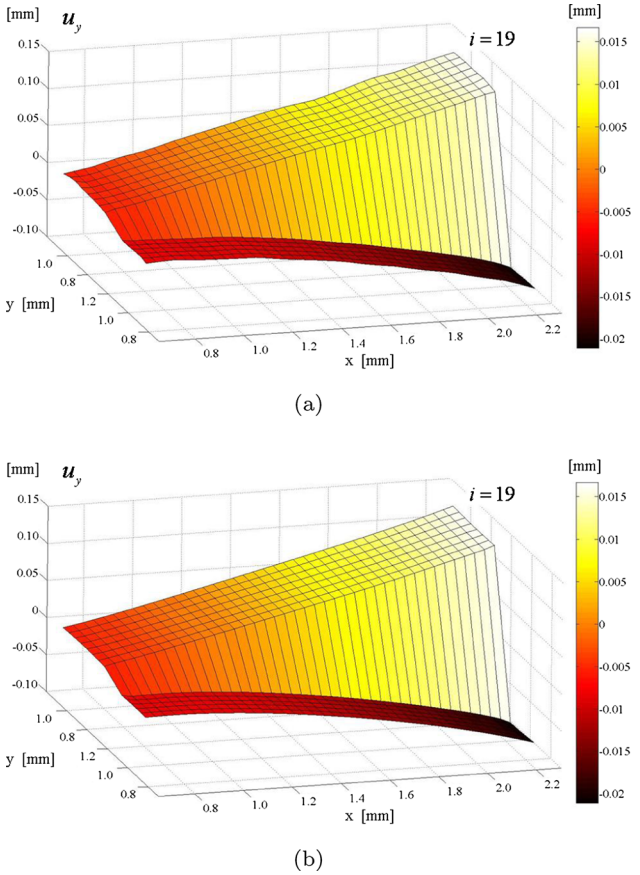

Fig. 7 Vertical displacement component (normal to the joint) computed by the FE model at instant $i = 19$, estimated by: the original identification procedure, in **(a)**; the extended strategy, in **(b)**

fields, being ± 0.1, ± 0.2 and ± 0.3 pixel the 99 % confidence intervals of additive perturbations. Even in the presence of noise, stabilization of the parameter estimates and relevant objective functions was observed after a few steps ($k = 5 \div 6$). The stopping criterion utilizes objective function evaluations at two subsequent steps: their percentage difference is compared with a threshold tuned by the user. In the numerical campaign, at the end of the identification procedures, objective functions in equations (7) and (8) attained values markedly lower than those exhibited at the beginning of the inverse analyses (at $k = 1$), as documented in Table 1. Resulting estimates of cohesive parameters together with the correct values assumed a priori are reported in Table 2, including also average percentage errors (per single parameter). In Table 3 the estimated displacement fields are compared with their noiseless counterparts (known a priori), on the basis of the maximum and average value of normalized discrepancies, before and after the identification procedure (at $k = 1$ and $k = 9$, respectively). For all the considered exercises, the identification procedure provided boundary displacements closer to the correct values than the initial noisy data, with an average normalized discrepancy of a few percentages, whilst the estimation error on each cohesive parameter never exceeded 15 %. In conclusion, the identification results provided by the extended procedure on the basis of pseudo-experimental data can be considered rather satisfactory, in terms of estimate stability and robustness with respect to noise.

Experimental data In the original, not regularized identification procedure of equation (5), estimates of mechanical parameters for the joint, gathered in vector $\widehat{\boldsymbol{x}}^{\mathrm{NR}} = \{\widehat{\phi}_n, \widehat{\delta}_n, \widehat{\delta}_n\}^T$, resulted as follows: $\widehat{\phi}_n = 2.32$ [GPa·μm], $\widehat{\delta}_n = 8.56$ [μm], $\widehat{\delta}_t = 84.8$ [μm]. It is worth noting that for such basic formulation the FE simulations were driven by noisy displacements $\boldsymbol{u}^{\mathrm{exp}}_{\partial\Omega}$ provided by DIC and *deterministically* prescribed along the boundary of the discretized subdomain. Indeed noise oscillations can be noted when focusing on the boundary nodes in Figs. 4(a) and 5(b) as for the horizontal displacement component (parallel to the joint), and in Figs. 6(a) and 7(a) for the vertical deformation (normally to the joint). In particular, at instant $i = 7$ vertical

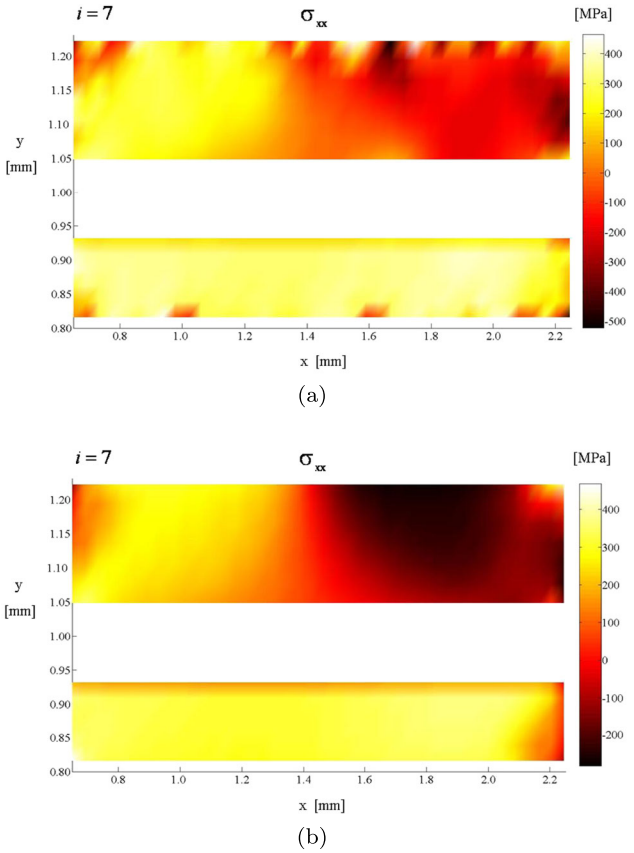

Fig. 8 Stress component σ_{xx} over the adherents computed by the FE model at instant $i = 7$, estimated by: the original identification procedure, in (**a**); the extended strategy, in (**b**)

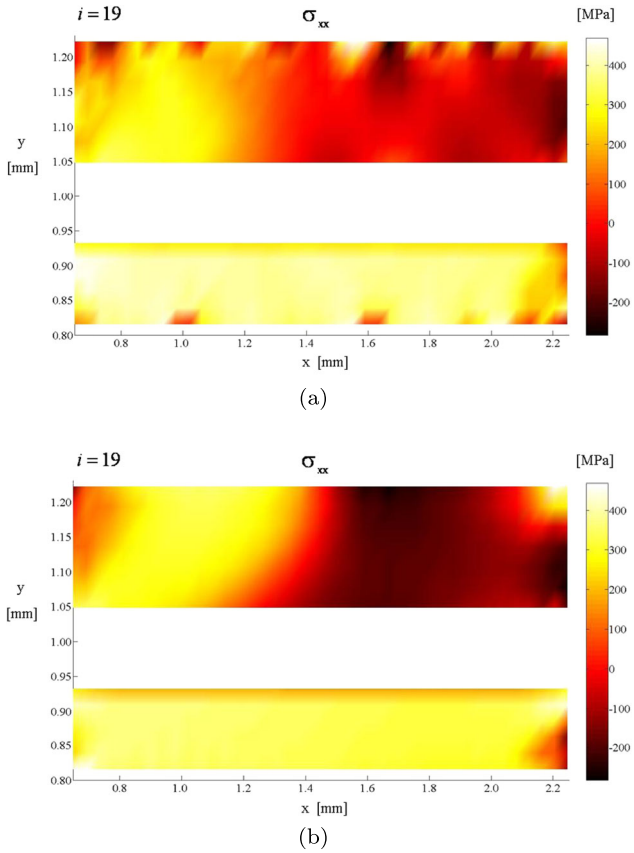

Fig. 9 Stress component σ_{xx} over the adherents computed by the FE model at instant $i = 19$, estimated by: the original identification procedure, in (**a**); the extended strategy, in (**b**)

displacements turn out to be small in absolute value, and the presence of important (in percentage) noise perturbations is not surprising. Because of the nonlinear behavior of the metal adherents, high frequency fluctuations due to noise propagate from the outer boundary into the subdomain, and are not rapidly attenuated as occurs in linear elasticity. The slender geometry of the monitored subdomain worsens this situation. As a confirmation of this, spurious peaks of stress without physical meaning can be observed closely to the outer border $\partial\Omega$, see Figs. 8(a) and 9(a) for the component σ_{xx} at instant $i = 7$ and 19, respectively. The same fluctuations can be recognized for the traction profiles along the joint, even though someway attenuated: the simplified kinematics of the adopted interface elements, with only two deformation modes (peel and shear), play herein a beneficial role acting as an implicit regularization.

As for the traction component normally to the joint, in Fig. 10(a) bell-shaped softening profiles in tension ($\Delta_n > 0$) can be clearly recognized, with a negligible noise-to-signal ratio. On the contrary, along the compressed part of the joint ($\Delta_n < 0$), marked oscillations appear ahead of the crack tip. As mentioned in [1], in compression the normal response of the finite-thickness interface was assumed to be linearly elastic (with a continuous slope at the origin), and decoupled from the tangential response: therefore the stress oscillations in compression passively follow the underlying strain field. Significant shear displacements develop along the joint from the very beginning of the test, and in percentage noise turns out to be less evident for this component and relevant traction, see Fig. 10(b). Relative displacements tangentially to the joint achieve the maximum value of about 105 μm at instant $i = 19$, being however small the difference between instants $i = 7$ and $i = 19$, as it can be ascertained by comparing Figs. 4(a) and 5(a), respectively. The normal displacements instead monotonically increase during the test, up to achieve at the final instant $i = 19$ a (relative) opening displacement of about 190 μm, at the right end of the joint, see Fig. 7(a). As a consequence, mode mixity turns out to vary continuously during the test.

In the extended and regularized identification procedure, equations (7) and (8), the initialization (at step $k = 1$) for the vector of interface parameters is provided by a reasonable guess $\widehat{\boldsymbol{x}}_0$, whilst boundary conditions are set equal to the experimental displacements $\boldsymbol{u}_{\partial\Omega}^{\exp}$ and *frozen* during

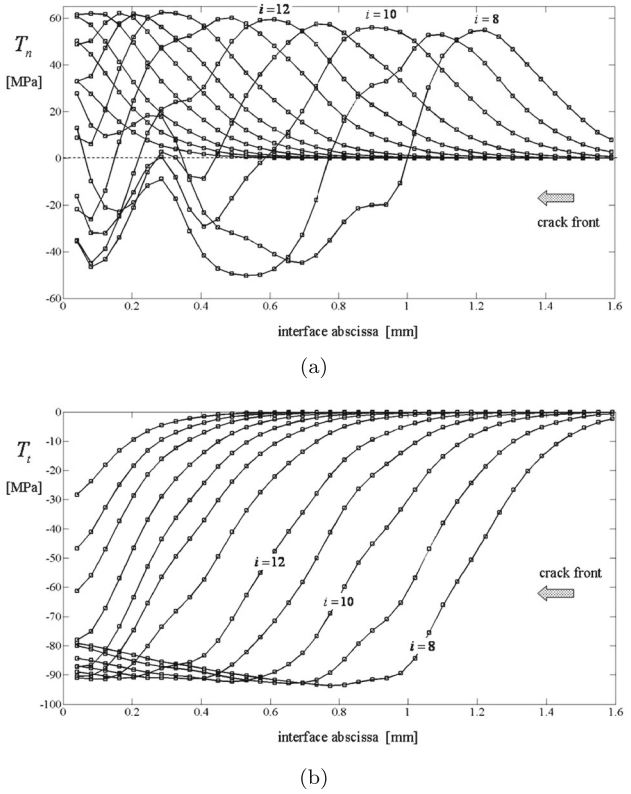

Fig. 10 Normal and tangential traction acting over the joint, in (**a**) and (**b**) respectively, provided by the original identification procedure at different instants i during the test simulation ($i = 1, ..., n_t \equiv 19$)

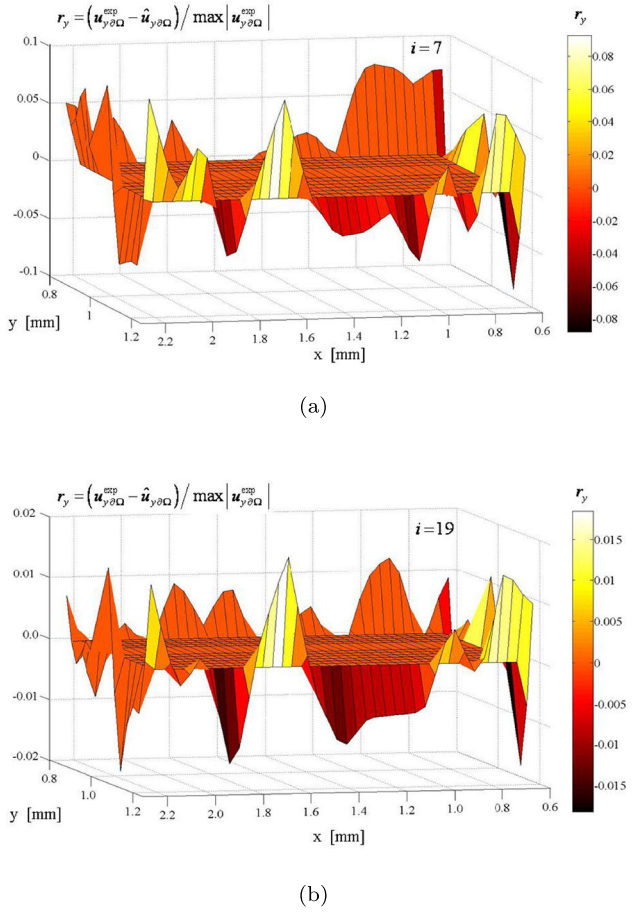

Fig. 11 Normalized discrepancy between the experimental vertical displacement along the boundary $u^{\exp}_{y\,\partial\Omega}$ and its estimate $\widehat{u}_{y\,\partial\Omega}$ by the extended procedure, at instants $i = 7$ and $i = 19$, in (**a**) and (**b**) respectively

Stage 1. Their roles are inverted during Stage 2. Mechanical parameters of the joint estimated by the extended regularized procedure are gathered in vector $\widehat{\boldsymbol{x}}^{\mathrm{R}} = \{\widehat{\phi}_n, \widehat{\delta}_n, \widehat{\delta}_n\}^T$, and resulted as follows: $\widehat{\phi}_n = 2.032$ [GPa·μm], $\widehat{\delta}_n = 8.721$ [μm], $\widehat{\delta}_t = 71.04$ [μm]. The change of the parameter values, with respect to the original estimates $\widehat{\boldsymbol{x}}^{\mathrm{NR}}$ defined above, was limited: a reduction of about 15 % can be observed for the work of separation ϕ_n and for the shear characteristic length δ_t, endowed by a small perturbation of the normal characteristic length δ_n.

By the proposed alternating minimization strategy, equations (7) and (8), also the boundary conditions prescribed to the discretized subdomain are iteratively updated at varying index k. The truncated basis entering the boundary data regularization term $R_u\left(\boldsymbol{u}^{\bar{i}}_{\partial\Omega}\right)$ in equation (8) relevant to $\bar{i}$-th time instant, is constituted of 10 Čebyšhëv polynomials, either dependent by one variable only or product of two one-dimensional functions. Such a basis has been selected after preliminary exercises, seeking a compromise between the minimum basis dimension and the best approximation of the underlying deformation fields. It should be regarded as a priori information, specifying the mathematical model [16]. However, the optimal dimension of the truncated basis can be selected also by applying Akaike's information criterion to the specific set of data, see e.g. [34]. Figure 11 shows the residuals computed by the extended procedure to correct the DIC-measured boundary displacements, expressed at time instant i by the the normalized discrepancy $r^i_y = \left(u^{i\,\exp}_{y\,\partial\Omega} - \widehat{u}^i_{y\,\partial\Omega}\right) / \max|u^{i\,\exp}_{y\,\partial\Omega}|$. As expected, correction r_y, which exhibits a variable sign along the boundary, is more significant at instant $i = 7$ (Fig. 11(a)), where peaks of 8 % can be observed, whilst it becomes negligible at the last instant $i = 19$, where it does not exceed $1 \div 2$ %, see Fig. 11(b). From the wavelengths of boundary residual profiles, it is possible to recognize functional terms included into the truncated basis, defined in the square $[-1, 1]^2$ and then mapped into the specific geometry (separately for the two adherents). In fact, higher order Čebyšhëv polynomials were selected along the direction parallel to the joint, and low order ones normally to the joint (through the height of the aluminum layers), plus some coupling terms.

The Neumann condition R_x along the cracked part of the joint is prescribed exclusively at instant $i = 9$ at the

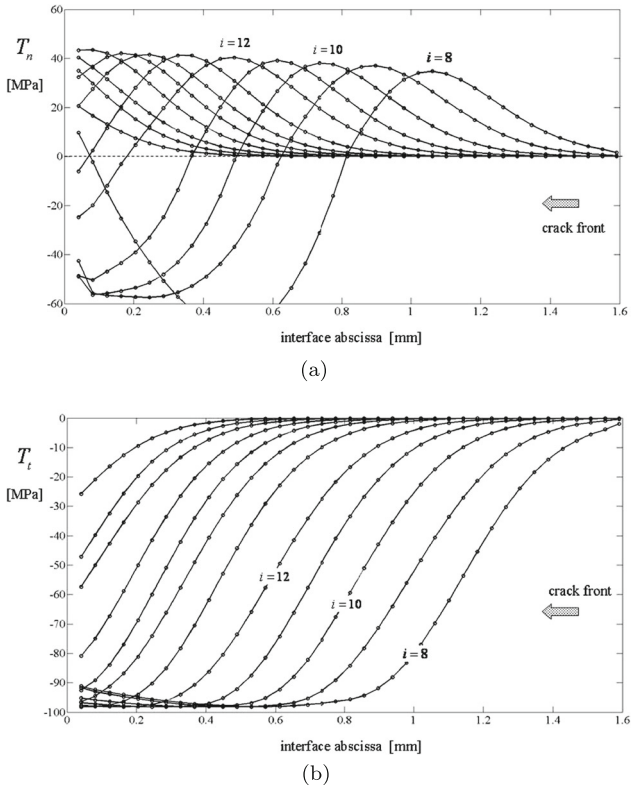

Fig. 12 Normal and tangential traction acting over the joint, in (**a**) and (**b**) respectively, provided by the extended identification procedure at different instants i during the test simulation ($i = 1, ..., n_t \equiv 19$)

right end of the modeled joint, where a macroscopic crack appeared in the available pictures. This local condition was satisfied at all the subsequent instants, even though not explicitly prescribed. This circumstance confirms that the crack front propagates monotonically from the right toward the left end of the modeled interface (as emphasized by the arrow in Fig. 12).

In the extended strategy the stress distributions turn out to be significantly smooth, as shown in Figs. 8(b) and 9(b) for the stress component σ_{xx}, and high frequency oscillations closely to the joint disappeared. Also interface tractions exhibit a more regular profile, as depicted in Fig. 12. If compared with the predictions of the original procedure (generated by estimates $\widehat{\boldsymbol{x}}^{\mathrm{NR}}$, see Fig. 10), the joint response along the tangential direction exhibits a 10% increment in modulus, with a difference of about 9 [MPa], as resulting in Fig. 12(b), being the shear strength dependent on the ratio ϕ_n/δ_t. Simultaneously, the normal strength in tension is reduced, see Fig. 12(a). In particular, maximum value of normal traction along the joint, achieved at instant $i = 16$, is significantly lower than before (max $T_n^{\mathrm{R}} = 43.4$ [MPa] versus max $T_n^{\mathrm{NR}} = 62.4$ [MPa]), whilst the compressive normal stresses for the considered instants turn out to be higher in modulus of about the same quantity.

Table 4 Truly experimental data. Estimates of joint mechanical parameters $\widehat{\boldsymbol{x}}^{\mathrm{R}}$ at varying the penalty coefficient c_x in equation (7) for the Neumann condition, being fixed the threshold vector $\boldsymbol{c}_F$ and penalty coefficient $c_u = 10^6$

c_x	ϕ_n [GPa · μm]	δ_n [μm]	δ_t [μm]
10^{+10}	2.032	8.721	71.04
10^{+6}	2.054	8.704	70.49
10^{+2}	1.932	9.123	64.37
0	5.841	168.4	141.8

It is worth emphasizing that the two regularization provisions detailed above play a crucial role in order to stabilize the parameter estimates against data perturbations. In the absence of the equilibrium condition R_x, identification results exhibit a lack of physical meaning, endowed by parameter values very far from those predicted by the original procedure due to the problem ill-posedness. In fact, when $c_x = 0$ is assumed (see Table 4), a large increase of the characteristic lengths δ_n and δ_t is observed. Predicted tractions do not vanish anymore along the joint and, remarkably, only slightly descending branches can be observed where complete debonding was instead expected. Moreover, whilst the maximum value of tangential traction T_t still appears reasonable (due to the marked increase of ϕ_n), the normal traction T_n reduces to a few MPa. The main mechanical features of the process in point (softening, debonding) are indeed lost, and even mode mixity is altered. When instead the constraint on boundary displacements R_u in equation (10) is relaxed by decreasing its penalty coefficient c_u (see Table 5), high-frequency noise appears again closely to the outer boundary, and, with it, the resulting stress distributions inside the ROI are corrupted, exactly as in the original approach.

Closing Remarks and Future Prospects

In this study, an extended inverse methodology was developed on the basis of kinematic measurements provided

Table 5 Truly experimental data. Estimates of joint mechanical parameters $\widehat{\boldsymbol{x}}^{\mathrm{R}}$ at varying penalty coefficient $\boldsymbol{c}_u$ in equation (8) for boundary data regularization, being fixed the threshold $\boldsymbol{c}_F$ for the Neumann condition and its penalty coefficient $c_x = 10^{10}$

c_u	ϕ_n [GPa · μm]	δ_n [μm]	δ_t [μm]
10^{+6}	2.032	8.721	71.04
10^{+2}	1.809	8.933	82.32
10^{-4}	1.834	8.892	81.46
10^{-8}	1.833	8.893	81.44

by 2D Digital Image Correlation (DIC), and it was used to assess the mechanical properties of an adhesive joint inside a bonded assembly for aerospace applications. A local approach was considered, focusing on a small subdomain over the sample surface monitored during mixed mode experiments, discretized by finite elements under plane stress conditions and driven by prescribed boundary conditions. The problem of reconstructing the "actual" boundary displacements for such subdomain, and that of estimating the mechanical parameters of joints or interfaces inside the industrial manufact, were tackled simultaneously in a coupled framework.

A suitable minimization strategy based on alternating directions was proposed to drastically reduce the high dimensionality of the extended inverse problem, exceeding a few thousand unknowns. Restricted (or partial) minimizations were performed, decoupling in each step the estimation of cohesive parameters (time independent) and that of boundary displacements at different instants along the test. To increase robustness of the inverse procedure, regularizing provisions were effectively implemented through original formulations. The regularization terms, added as penalty factors in the objective functions to minimize, enforced smoothness of boundary displacements and equilibrium along the debonded part of the joint. The procedure was preliminarily assessed by synthetic data with different signal-to-noise ratios. When truly experimental data were processed, the results in terms of traction profiles along the joint and of stress distributions over the adherends turned out to be rather satisfactory.

It is worth emphasizing that, by the proposed approach, code for 2D Digital Image Correlation was dealt with as a black box, and raw digital images were processed independently from the mechanical model and without any regularization provision (besides those intrinsic to the Galerkin formulation adopted for DIC). As a further ambitious development, corroborated by several partial attempts proposed in the recent literature (see e.g. [35]), a coupled framework can be considered, including in a consistent fashion the optical inverse problem, the mechanical forward operator and the identification of governing parameters. By such a computational strategy, all the available information from different sources and with diverse uncertainties could be synergistically combined, exploited for mutual regularization, and the global errors and residuals rigorously assessed.

Acknowledgments The Author kindly acknowledges the support provided by CARIPLO Foundation to the Project titled: "Innovative metal-ceramic joints for high and ultra-high temperature applications (UHT)" (Grant n. 2010-0432, Call for Scientific and technological research on advanced materials). The contribution to this study provided by Dr. Eng. Roberta Santoro is gratefully acknowledged.

Appendix

Plane Stress and Plane Strain Approximations

In the present Appendix a comparative assessment of the plane strain and plane stress approximations applied to the discretized domain was summarized for the readers' convenience. Additional forward simulations were performed on the ROI subjected to a mechanical test with a different configuration. As shown in Fig. 13, the ROI model was encastred at the left end, and a concentrated load was applied at the right upper corner (a force per unit out-of-plane thickness). The increasing loading generated stresses and strains in the elastic-plastic adherents, and mixed mode loading conditions inside the joint. Plane stress and plane strain conditions were alternatively assumed, while the cohesive properties of the adhesive joint remained the same. As expected, discrepancy between displacements computed under plane stress and those predicted under plane strain increases with the applied loading, being however the plane strain solution more stiff: in Fig. 13, the applied force f per unit thickness is plotted as a function of resulting displacement at the application point B, and the relevant deformed meshes are comparatively shown (the dashed line in the force-displacement plot indicates the current force value). These additional simulations made available further synthetic data concerning a different configuration, both under plane strain and under plane stress conditions.

(i) In the first exercise, displacements generated by the above experiment under plane strain conditions were used to perform inverse analyses. In particular, during the identification procedure displacements at the nodes along the boundary were used to drive plane strain simulations of the ROI, while displacements inside the ROI generated through the same forward analyses (i.e. with the plane strain approximation of the specimen in Fig. 13) entered the objective function to minimize as comparison terms. In this case the cohesive parameters $\boldsymbol{x}$ of the joint were correctly estimated, and no difference was observed with respect to the plane stress exercises discussed in the paper.

(ii) Thereafter, kinematic data generated by the novel test in Fig. 13 under plane stress conditions were applied to drive simulations of the ROI according to the plane strain assumption: in other terms, plane stress displacements were used to drive plane strain analyses as prescribed boundary conditions, and also were included in the objective function as comparison terms. The coupling of plane stress kinematic data with plane strain simulations has led to estimates of

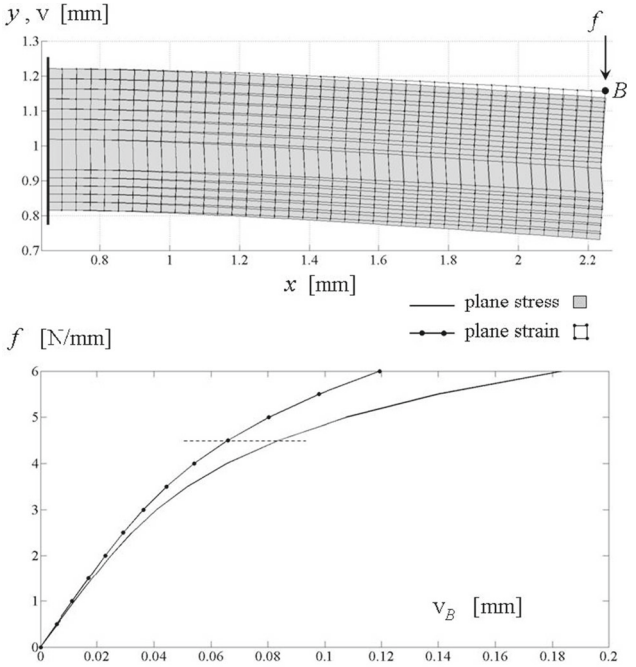

Fig. 13 Simulation of a novel mechanical test on the region of interest under plane strain and plane stress conditions: deformed meshes (dashed line indicates the current force value) and relevant responses in terms of applied force f (per unit out-of-plane thickness) and vertical displacement of the application point B

cohesive parameters which result very different from the values assumed a priori in the specimen of Fig. 13, and moreover generate along the joint unrealistically high tractions.

(iii) Finally, to further corroborate the work done, kinematic fields provided by the novel test under plane stress conditions were used (as in the paper) to drive the simulations of the ROI according to the plane stress approximation. Also in this case, all the cohesive parameters were correctly estimated.

References

1. Fedele R, Raka B, Hild F, Roux S (2009) Identification of adhesive properties in GLARE laminates by Digital Image Correlation. J Mech Physics Solids 57(7):1003–1016
2. Sutton M, Orteu J, Schreier H (2009) Image correlation for shape motion and deformation measurements. Springer-Verlag, Heidelberg
3. Espinosa H, Hild F (2012) IUTAM Symposium on Full-field Measurements and Identification in Solid Mechanics. Cachan, France 4-8 July 2011 Procedia IUTAM, vol 4. Elsevier BV Dordrecht, The Netherlands
4. Grediac M, Hild F (eds) (2013) Full-field Measurements and Identification in Solid Mechanics. John Wiley & Sons, Hoboken (US) ISTE Ltd London
5. Shen B, Paulino G (2011) Identification of cohesive zone model and elastic parameters of fiber-reinforced cementitious composites using digital image correlation and a hybrid inverse technique. Cem Concr Comp 33:572–585
6. Guerrero M, Martinez M, Picon R, Marante ME, Hild F, Roux S, Florez-Lopez J (2013) Experimental analysis of masonry infilled frames using digital image correlation. Mater Struct May. doi:10.1617/s11527-013-0099-0
7. Ghiassi B, Xavier J, Oliveira DV, Lourenço PB (2013) Application of Digital Image Correlation in Investigating the Bond Between FRP and Masonry. Comp Struct 106: 340–349
8. Fedele R, Scaioni M, Barazzetti L, Rosati G, Biolzi L (2014) Delamination tests on CFRP-reinforced masonry pillars: optical monitoring and mechanical modelling. Cem Concr Comp 45:243–254
9. Pan B, Wu D, Gao J (2013) High-temperature strain measurement using active imaging digital image correlation and infrared radiation heating. J Strain Anal Eng Design September. doi:10.1177/0309324713502201
10. Leplay P, Réthoré J, Meille S, Baietto MC (2012) Identification of asymmetric constitutive laws at high temperature based on Digital Image Correlation. J Eur Ceramic Soc 32:3949–3958
11. Ki HG, Chew HB, Kim KS (2012) Inverse extraction of cohesive zone laws by field projection method using numerical auxiliary fields. Int J Numer Meth Engn 91:516–530
12. Mathieu F, Aimedieu P, Guimard JM, Hild F (2013) Identification of interlaminar fracture properties of a composite laminate using local full-field kinematic measurements and finite element simulations. Comp Part A 49:203–213
13. Réthoré J, Estevez R (2013) Identification of a cohesive zone model from digital images at the micron-scale. J Mech Physics Solids 61:1407–1420
14. Richefeu V, Chrysochoos A, Huon V, Monerie Y, Peyroux R, Wattrisse B (2012) Toward local identification of cohesive zone models using digital image correlation. Eur J Mech-A/ Solids 34(4):38–51
15. Fedele R, Filippini M, Maier G (2005) Constitutive model calibration for railway wheel steel through tension-torsion tests. Comp and Struct 83:1005–1220
16. Fedele R, Maier G, Whelan M (2006) Calibration of local constitutive models through measurements at the macroscale in heterogeneous media. Comp Meth Appl Mech Engn 195(37):4971–4990
17. Fedele R, Maier G (2007) Flat-jack tests and inverse analysis for the identification of stress states and elastic properties in concrete dams. Meccanica 42(4):387–402
18. Kolluri M, Hoefnagels JPM, van Dommelen JAW, Geers MGD (2011) An improved miniature mixed-mode delamination setup for *in situ* microscopic interface failure analyses. J Phys D: Appl Phys 44. doi:10.1088/0022-3727/44/3/034005
19. Bornert M, Brémand F, Doumalin P, Dupré J, Fazzini M, Grédiac M, Hild F, Mistou S, Molimard J, Orteu J, Robert L, Surrel Y, Vacher P, Wattrisse B (2009) Assessment of digital image correlation measurement errors: methodology and results. Exp Mech 49:353–370
20. Moriniére FD, Alderliesten RC, Tooski MY, Bemedictus R (2012) Damage evolution in GLARE fibre-metal laminate under repeated low-velocity impact tests. Cent Eur J Engn 2(4):603–611
21. Besnard G, Hild F, Roux S (2006) Finite-element displacement fields analysis from digital images: Application to Portevin-Le Châtelier bands. Exp Mech 46:789–803
22. Mücke R, Bernhardi OE (2003) A constitutive model for anisotropic materials based on Neuber's rule. Comp Meth Appl Mech Eng 192:4237–4255

23. Van den Bosch MJ, Schreurs PJG, Geers MGD (2006) An improved description of the exponential Xu and Needleman cohesive zone law for mixed-mode decohesion. Eng Fract Mech 73:1220–1234
24. Balzani C, Wagner W (2008) An interface element for the simulation of delamination in unidirectional fiber-reinforced composite laminates. Eng Fract Mech 75(9): 2597–2615
25. Samimi M, van Dommelen JAW, Kolluri M, Hoefnagels JPM, Geers MGD (2013) Simulation of interlaminar damage in mixed-mode bending tests using large deformation self-adaptive cohesive zones. Eng Fract Mech 109(9): 387–402
26. Fedele R, Ciani A, Galantucci L, Bettuzzi M, Andena L (2013) A regularized, pyramidal multi-grid approach to global 3D-Volume Digital Image Correlation based on X-ray micro-tomography. Fund Inform 125(3–4):361–376
27. Chen X, Deng X, Sutton MA, Zavattieri P (2014) An inverse analysis of cohesive zone model parameter values for ductile crack growth simulations. Int J Mech Sci 79: 206–215
28. Kleiber M, Antunez H, Hien TD, Kowalczyk P (1997) Parameter Sensitivity in Nonlinear Mechanics. Theory and Finite Element Computations. John Wiley Sons, New York USA
29. Bonnet M, Frangi A (2006) Analyse des solides déformables par la méthode des éléments finis. Les Editions de l'Ecole Polytechnique, Palaiseau France
30. Byrne CL (2013) Alternating Minimization as Sequential Unconstrained Minimization: A Survey. J Optim Theory and Appl 156(3):554–566
31. Matlab 9.1 R13 (2013) Optimization Toolbox Manual. The MathWorks Inc
32. Giannessi F, Pallaschke D, Rubinov AM (2005) Optimization. Taylor and Francis, London
33. Canuto C, Hussaini MY, Quarteroni A, Zang TA (2006) Spectral Methods. Fundamentals in Single Domains Springer Series in Computational Mathematics vol 23. Springer-Verlag, Berlin, Heidelberg
34. MacKay DJC (2003) Information Theory, Inference and Learning Algorithms. Cambridge University Press, New York
35. Leclerc H, Périé JN, Roux S, Hild F (2011) Voxel-Scale Digital Volume Correlation. Exp Mech 51:479–490